ACS OMEGA

http://pubs.acs.org/journal/acsodf

Article

Hydrodynamics of Irregular-Shaped Graphite Particles in Coaxial Two-Phase Jet Flow

Yang Liu,* Guohui Li,* Yongju Zhang, and Li Zhang

Cite This: *ACS Omega* 2021, 6, 16631−16640

Read Online

ACCESS | Metrics & More | Article Recommendations

ABSTRACT: Expanded graphite particle is characterized by the low density in comparison with those of bead glass and copper particles. Hydrodynamics of the irregular-shaped graphite particle swirling flows in a coaxial chamber are investigated via an improved kinetic frictional stress model. A drag force coefficient considering the effects of irregular shapes based on the artificial neural network algorithm is adopted to describe the momentum transfer between nonspherical particles and gas phases. The proposed model, algorithm, and source code for modeling and simulation are validated by measurement using spherical glass beads, and acceptable agreement is obtained. Lower sphericity particles enhance the anisotropic particle dispersions and induces the redistributions of the Reynolds stresses of the two-phase flow. Irregular-shaped particles are more sensitive to the gas followability instead of own inertia, whereas spherical particles are easier to be affected by the inlet effects. The interlock force between nonspherical particles takes great effect on particle flow than the spherical particle. The axial−axial normal stresses of sphericities of 0.63 and 0.72 are approximately 3.4 times larger than those of shear stress of spherical particle, and their axial velocities locating at near central regions are 3.0 times larger than those of sphericities.

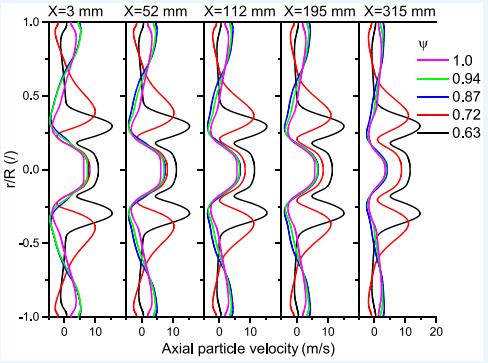

INTRODUCTION

A fullerene is a kind of important material that has been applied in the fields of superconductivity, advanced function materials, and nanotechnology. The combustion-synthesized strategy to fabricate the fullerene based on the expanded graphite particle (EGP) has been developed rapidly in recent years. However, the gas-particle two-phase hydrodynamics and combustion process are significantly determined by particle properties and dispersion behaviors.[1,2] Expanded graphite particles have loose, porous internal structures with a relatively lower density in the order of 10−100. Compared to the conventional density particles ($\sim 10^3$), they have unique dispersion characteristics, especially in a swirling combustor as a result of the complicated transport process, turbulent mixing, diffusion, and unclear illustrations regarding the interaction mechanism between particle and gas phases. The formation of recirculation and primary circulation regions has great effects on the intensity of momentum, heat, and mass transfer and the turbulent flow structure.[3−8] In many combustion devices, swirling flow is used to stabilize the flame depending on the recirculation zones. Swirling flow is easier to incur the instabilities, leading to triggering combustion oscillations and deteriorating performances. The amounts of recirculation regions and central vortex breakdown zones are relied on the swirling strength in many swirl-stabilized flames represented by the highly anisotropic, large-scale turbulent structure with shear flow regions. Therefore, it is necessary to gain a better understanding with regard to the particle anisotropic dispersion characteristics and momentum interaction mechanism between the gas and particle phases.

Experimental studies for swirling gas−particle flows using the particle image velocity,[9−12] the phase Doppler particle analyzer,[6,7,13] the laser digital velocity,[14] and so forth have been successfully utilized to capture the particle dispersions in swirling gas−particle turbulent flows. However, majority of studies focus on the dispersion of spherical particles rather than on nonspherical particles. The computational fluid dynamics method has been rapidly developed because it is the most potential and cost-effective way to not only reveal the basic hydrodynamics but also explore their application conveniently. Generally, a simulation algorithm is classified into the Euler−Euler two-fluid model (TFM)[15−19] and the Euler−Lagrange discrete particle model (DPM).[20−24] As for TFM, both gas and particle phases are considered as the continuum and full interpenetration of each other, which is dominantly popularized for a large-scale simulation due to a

Received: April 17, 2021
Accepted: June 8, 2021
Published: June 16, 2021

https://doi.org/10.1021/acsomega.1c02053
ACS Omega 2021, 6, 16631−16640

Table 1. Mathematical Model of Irregular-Shaped Particle Swirling Two-Phase Flow

	A: Conservation Equations	
(a) continuity equations		
gas phase	$\frac{\partial}{\partial t}(\alpha_g\rho_g) + \frac{\partial}{\partial x_j}(\alpha_g\rho_g\overline{u_{gi}}) = 0$	T-1
particle phase	$\frac{\partial}{\partial t}(\alpha_p\rho_p) + \frac{\partial}{\partial x_j}(\alpha_p\rho_p\overline{u_{pi}}) = 0$	T-2
(b) momentum equations		
gas phase	$\frac{\partial(\alpha_g\rho_g\overline{u_{gi}})}{\partial t} + \frac{\partial(\alpha_g\rho_g\overline{u_{gk}}\overline{u_{gi}})}{\partial x_k} = \alpha_g\rho_g g - \alpha_g\frac{\partial\overline{p}}{\partial x_i} + \frac{\partial}{\partial x_k}(\tau_{gik} - \alpha_g\rho_g\overline{u'_{gi}u'_{gk}}) - \beta_{gp}(\overline{u_{gi}} - \overline{u_{pi}})$	T-3
particle phase	$\frac{\partial(\alpha_p\rho_p\overline{u_{pi}})}{\partial t} + \frac{\partial(\alpha_p\rho_p\overline{u_{pk}}\overline{u_{pi}})}{\partial x_k} = \alpha_p\rho_p g - \alpha_p\frac{\partial\overline{p}}{\partial x_i} - \frac{\partial\overline{p_p}}{\partial x_i} + \frac{\partial}{\partial x_k}(\tau_{pik} - \alpha_p\rho_p\overline{u'_{pk}u'_{pi}}) + \beta_{pg}(\overline{u_{gi}} - \overline{u_{pi}})$	T-4
(c) equation of particle fluctuating energy	$\frac{3}{2}\left[\frac{\partial(\alpha_p\rho_p\theta)}{\partial t} + \frac{\partial(\alpha_p\rho_p\overline{u_{pk}}\theta)}{\partial x_k}\right] = (-\nabla p_p\bar{I} + \tau_p)\colon\nabla u_p + \nabla\cdot(\Gamma_p\nabla\theta) - \gamma_p + \varphi_p + D_{gp}$	T-5
	B: Constitutive Equations	
(a) Reynolds stress equation of gas phase	$\frac{\partial(\alpha_g\rho_g\overline{u'_{gi}u'_{gj}})}{\partial t} + \frac{\partial(\alpha_g\rho_g\overline{u_{gk}}\cdot\overline{u'_{gi}u'_{gj}})}{\partial x_k} = D_{g,ij} + P_{g,ij} + \Pi_{g,ij} - \varepsilon_{g,ij} + G_{g,gp,ij}$	T-6
(b) Reynolds stress equation of particle phase	$\frac{\partial(\alpha_p\rho_p\overline{u'_{pi}u'_{pj}})}{\partial t} + \frac{\partial(\alpha_p\rho_p\overline{u_{pk}}\cdot\overline{u'_{pi}u'_{pj}})}{\partial x_k} = D_{p,ij} + P_{p,ij} + \Pi_{p,ij} - \varepsilon_{p,ij} + G_{p,gp,ij}$	T-7
(c) turbophoresis force	$D_{p,ij} = \frac{\partial}{\partial x_k}\left(C_s\alpha_p\rho_p\frac{k_p}{\varepsilon_p}\overline{u'_{pk}u'_{pl}}\frac{\partial\overline{u'_{pi}u'_{pj}}}{\partial x_l}\right)$	T-8
(d) particle shear production	$P_{p,ij} = -\alpha_p\rho_{pm}\left(\overline{u'_{pk}u'_{pj}}\frac{\partial\overline{u_{pi}}}{\partial x_k} + \overline{u'_{pk}u'_{pi}}\frac{\partial\overline{u_{pj}}}{\partial x_k}\right)$	T-9
(e) particle pressure−strain	$\prod_{p,ij} = \prod_{p,ij,1} + \prod_{p,ij,2} = -C_{p1}\frac{\varepsilon_p}{k_p}\alpha_p\rho_p\left(\overline{u'_{pi}u'_{pj}} - \frac{2}{3}k_p\delta_{ij}\right) - C_{p2}\left(P_{p,ij} - \frac{2}{3}P_p\delta_{ij}\right)$	T-10
(f) particle dissipation	$\varepsilon_{p,ij} = \frac{2}{3}\delta_{ij}\alpha_p\rho_p\varepsilon_p$	T-11
(g) two-phase interaction	$G_{p,gp,ij} = \beta_{gp}(\overline{u'_{pi}u'_{gj}} + \overline{u'_{pj}u'_{gi}} - 2\overline{u'_{pi}u'_{pj}})$	T-12
(h) equation of gas-particle interphase Reynolds stress	$\frac{\partial\overline{u'_{pi}u'_{gj}}}{\partial t} + (\overline{u_{gk}} + \overline{u_{pk}})\frac{\partial\overline{u'_{pi}u'_{gj}}}{\partial x_k} = D_{gp,ij} + P_{gp,ij} + \Pi_{gp,ij} - \varepsilon_{gp,ij} + T_{gp,ij}$	T-13
(i) interphase diffusion	$D_{gp,ij} = \frac{\partial}{\partial x_k}\left(C_{gp,3}\left(\frac{k_p}{\varepsilon_p}\overline{u'_{pk}u'_{pl}} + \frac{k_g}{\varepsilon_g}\overline{u'_{gk}u'_{gl}}\right)\frac{\partial\overline{u'_{gi}u'_{pj}}}{\partial x_l}\right)$	T-14
(j) interphase shear production	$P_{gp,ij} = -\overline{u'_{pi}u'_{gk}}\frac{\partial\overline{u_{gj}}}{\partial x_k} - \overline{u'_{pk}u'_{gj}}\frac{\partial\overline{u_{pi}}}{\partial x_k}$	T-15
(k) interphase pressure−strain	$\prod_{gp,ij} = \prod_{gp,ij,1} + \prod_{gp,ij,2} = -\frac{C_{gp,1}}{\tau_{rp}}\left(\overline{u'_{pi}u'_{gj}} - \frac{2}{3}k_{gp}\delta_{ij}\right) - C_{gp,2}\left(P_{gp,ij} - \frac{2}{3}P_{gp}\delta_{ij}\right)$	T-16
(l) interphase dissipation	$\varepsilon_{gp,ij} = \frac{\overline{u'_{pi}u'_{gj}}}{\min\left(\tau_{rp}, \frac{k_g}{\varepsilon_g}\right)}$	T-17
(m) interphase interaction	$T_{gp,ij} = \frac{\beta}{\alpha_g\rho_g\alpha_p\rho_p}(\alpha_p\rho_p\overline{u'_{pi}u'_{pj}} + \alpha_g\rho_g\overline{u'_{gi}u'_{gj}} - (\alpha_g\rho_g + \alpha_p\rho_p)\overline{u'_{gj}u'_{pi}})$	T-18
(n) granular temperature	$\theta = \frac{1}{3}(\overline{u'_{pi}u'_{pi}} + \overline{u'_{pj}u'_{pj}} + \overline{u'_{pk}u'_{pk}})$	T-19
(o) translational fluctuation energy dissipation rate	$\gamma_p = 3(1 - e_{eff}^2)\alpha_p^2\rho_p g_0\theta\left(\frac{4}{\phi d_p}\sqrt{\frac{\theta}{\pi}}\right)$	T-20
(p) bulk particle viscosity	$\xi_p = \frac{4}{3}\alpha_p^2\rho_p\phi d_p g_0(1 + e_{eff})\sqrt{\frac{\theta}{\pi}}$	T-21
(q) particle stress	$\tau_p = (\xi_p\nabla\cdot u_p)I + \mu_p\left\{[\nabla u_p + (\nabla u_p)^T] - \frac{1}{3}(\nabla u_p)I\right\}$	T-22
(r) conductivity coefficient of granular temperature	$\Gamma_p = \frac{150}{384(1 + e_{eff})g_0}\rho_p\phi d_p\sqrt{\pi\theta}\left[1 + \frac{6}{5}(1 + e_{eff})g_0\alpha_p\right]^2 + 2\alpha_p^2\rho_p\phi d_p g_0(1 + e_{eff})\sqrt{\frac{\theta}{\pi}}$	T-23
(s) effective coefficient of particle restitution	$e_{eff} = e - \frac{a_1}{2} + \frac{a_2 b_1}{2b_2}$	T-24
(t) net fluctuation energy exchange	$\varphi_p = -3\beta_{gp}\theta$	T-25
(u) rate of energy dissipation	$D_{gp} = \frac{\phi d_p\rho_p}{4\sqrt{\pi\theta}}\left(\frac{18\mu_g}{(\phi d_p)^2\rho_p}\right)\lvert u_g - u_p\rvert^2$	T-26
(v) particle pressure	$p_p = \alpha_p\rho_p[1 + 2(1 + e_{eff})\alpha_p g_0]\theta + p_p^f$	T-27
(w) radial distribution function	$g_0 = \left[1 - \left(\frac{\alpha_p}{\alpha_{p,max}}\right)^{1/3}\right]^{-1}$	T-28

https://doi.org/10.1021/acsomega.1c02053
ACS Omega 2021, 6, 16631−16640

Table 1. continued

	B: Constitutive Equations	
(x) particle relax time	$\tau_{rs} = d_p^2\rho_p\left(1 + \frac{Re_p^{2/3}}{6}\right)^{-1}/18\mu_g$	T-29
(y) particle viscosity	$\mu_p = \frac{2\mu_{p,dil}}{(1+e_{eff})g_0}\left[1 + \frac{4}{5}(1+e_{eff})g_0\alpha_p\right]^2 + \frac{4}{5}\alpha_p^2\rho_p\phi d_p g_0(1+e_{eff})\sqrt{\frac{\theta}{\pi}} + \mu_p^f$	T-30
	$\mu_{p,dil} = \frac{5}{96}\rho_p\phi d_p\sqrt{\pi\theta}$	T-31
	$I_{2D} = -\frac{1}{2}\left[\frac{1}{2}(\nabla u_p + \nabla u_p^T) - \frac{1}{3}(\nabla\cdot u_p)I\right]:\left[\frac{1}{2}(\nabla u_p + \nabla u_p^T) - \frac{1}{3}(\nabla\cdot u_p)I\right]$	T-32
frictional stress	$p_p^f = \begin{cases} 0 & \varepsilon_p \le \varepsilon_{p,min} \\ 0.05\frac{(\varepsilon_p - \varepsilon_{p,min})^2}{(\varepsilon_{p,max} - \varepsilon_p)^5} & \varepsilon_p \le \varepsilon_{p,min} \end{cases}$	T-33
(z) interphase momentum exchange coefficient		
Ergun model	$\beta_{Ergun} = 150\frac{\alpha_p(1-\alpha_g)\mu_g}{\alpha_g(\varphi d_p)^2} + 1.75\frac{\alpha_p\rho_g\lvert\overline{u_g} - \overline{u_p}\rvert}{\varphi d_p}$	T-34
Wen−Yu model	$\beta_{Wen,Yu} = \frac{3}{4}C_D\frac{\alpha_p\alpha_g\rho_g\lvert\overline{u_g} - \overline{u_p}\rvert}{d_p}\alpha_g^{-2.65}$	T-35
Huilin−Gidaspow model	$\beta_{pg} = (1-\varphi)\beta_{Ergun} + \varphi\beta_{Wen\text{-}Yu}$	T-36
	$\varphi = \frac{\arctan[150\times 1.75(0.2-\alpha_s)]}{\pi} + 0.5$	T-37
drag force coefficient	$\lg C_D = A_0 + A_1(\lg Re_p) + A_2(lg\ Re_p)^2 + A_3(lg\ Re_p)^3 + A_4(lg\ Re_p)^4$	T-38
	$\begin{pmatrix} A_0 \\ A_1 \\ A_2 \\ A_3 \\ A_4 \end{pmatrix} = \begin{pmatrix} -18.5047 & 183.2503 & -613.2826 & 966.0357 & -727.4302 & 211.3367 \\ -12.8162 & 75.0120 & -163.6044 & 150.0228 & -49.4788 & 0 \\ 0.9571 & -7.8929 & 22.3575 & -25.1512 & 9.8015 & 0 \\ 0.4725 & -3.0411 & 5.9850 & -4.2176 & 0.8038 & 0 \\ -0.0480 & 0.4531 & -1.0986 & 0.9621 & -0.2671 & 0 \end{pmatrix}\begin{pmatrix} 1 \\ \varphi \\ \varphi^2 \\ \varphi^3 \\ \varphi^4 \\ \varphi^5 \end{pmatrix}$	T-39
particle Reynolds number	$Re_p = \frac{\alpha_g\rho_g d_p\lvert\overline{u_g} - \overline{u_p}\rvert}{\mu_g}$	T-40

lower CPU time in comparison with DPM. Certainly, the necessary closure correlations for the Reynolds stress transport equations describing the interactions between gas and particle phases by using the two-way or four-way coupling methods are required. Based on the Reynolds-averaged Navier−Stokes (RANS) algorithm, a standard $k-\varepsilon$ turbulence model and the DPM for tracking the particle trajectory in swirling two-phase turbulence flow are used.[8] A two-phase second-moment turbulent model to numerically simulate the turbulent flow structure, the heat transfer of droplet-laden, gas−droplet, and gas-dispersed particle of separated/swirling flows in sudden expansion pipe was utilized. They found that the fine particle attenuates the gas turbulence up to 25%.[19,25] A unified second-order moment particle collision model to depict the anisotropic characteristics of particle, the redistributions of Reynolds stresses of two phases, and the mixing and separation behaviors was proposed.[26] The RANS cannot effectively obtain the coherent structure of turbulent flows and instantaneous velocity information. The high-fidelity simulation algorithm, the large eddy simulation, and the direct numerical simulation (DNS) have successfully performed the single-particle phase swirling and sudden expansion particle-laden hydrodynamics;[27−29] however, they are adopted for the merely spherical particle rather than the nonspherical particle. For the two-phase turbulent flow of nonspherical particles, a torque coefficient for the four kinds of nonspherical particle shapes with a wide range of flow of Reynolds numbers was developed.[30] As for DPM simulation, a new set of correlations of drag, lift, and torque coefficients for nonspherical single particle that was determined by the fitting DNS results for the flow around prolate ellipsoidal particles in a larger range of Reynolds number was established.[31,32] The total particle deposition increases with size and density, especially the ellipsoidal shape particles are more prone to the deposition for the turbulent swirling reacting flows.[33] Moreover, another finding is that the contributions of particle size distribution on dispersity effects are larger than the particle's shape. The particle size has a larger influence on the swirling coal particle pneumatic conveying than the irregular shape of particles.[34] Particle dispersion behavior is significantly differed from those of spherical and highly nonspherical particles in lateral particle distribution after injection into a vertical cross flow.[35]

The interaction between gas and spherical or nonspherical particles is calculated by the product of the drag coefficient and slip velocity. Most drag force correlations are always dependent on the spherical particle with homogeneous and heterogeneous empirical attributions that were derived from the existing drag equations.[36] Regarding nonspherical particles, a new drag force coefficient, which is a function of the particle Reynolds number and particle sphericity using the artificial neural model for nonspherical particle in a dense gas−particle two-phase flow, was proposed.[37,38] Meanwhile, effects of particle shapes on the hydrodynamics on the microscale level are revealed.[39−41] Until now, the effects of nonspherical particle shapes on particle dispersions in swirling two-phase flows have not been reported, especially for ultralight density particles. The aim of the present study is to explore the effects of irregular shape on the hydrodynamics of ultralight expanded graphite turbulent flows. The first proposed second-order moment model have successfully simulated the anisotropic dispersions of the particle and bubble and the hydrodynamics of gas−particle and bubble−particle two-phase flows.[3−5,42−46] In this work, a frictional kinetic stress coupling second-order moment model was improved to simulate the swirling nonspherical particle flow in a coaxial chamber. Momentum interactions between nonspherical particles and gas are described by Yan's model.[37]

https://doi.org/10.1021/acsomega.1c02053
ACS Omega 2021, 6, 16631−16640

Effects of particle sphericity on two-phase particle hydrodynamic dispersions are analyzed in detail.

MATHEMATICAL MODELING AND NUMERICAL ALGORITHM

The proposed frictional kinetic stress model based on the framework of the two-fluid approach is developed, in which the anisotropic dispersions of nonspherical particles are modeled by the two-phase Reynolds stress transport equations.[42] Conservation laws of mass and momentum are satisfied with each phase, and no mass and heat transfer occurred between gas and particle phases. Governing equations and their closure correlations, such as the mass conservation equations, the momentum transport equations, and the Reynolds stress equations, are listed in Table 1.

Governing Equations. Numerical Algorithm. The finite volume method is used to solve the governing equations, and computational domains are divided into the finite number of control volumes. Scalar parameters, including particle volume fraction, density, and turbulent kinetic energy, are stored in the center of control volume. The staggered grid arrangement to solve the velocity components located at the control volume surface is utilized. The semi-implicit pressure linked equation-corrected algorithm to correct the $p-v$ correlation with the tridiagonal marching algorithm by the line-by-line iteration, the under-relaxation quadratic upstream interpolation, and the convective kinematics procedure. In addition, the central difference scheme for the diffusion term is adopted to solve the finite differential equations. As for the inlet conditions, the particle inlet velocity is set to uniformity and the gas inlet velocity is set to the parabolic distribution. The normal and shear components of the Reynolds stress are assumed to be eddy-viscosity constants, and the inlet dissipation is given as $\varepsilon_{in} = c_\mu^{0.75} k_{in}^{1.5}/\lambda L$, where $c_\mu = 0.09$ and $\lambda = 0.07$. Full development outlet boundary and nonslip wall boundary conditions for gas velocity are employed. The Reynolds stresses are mainly determined by the production terms, and both axial gas and particle boundary conditions are symmetric. Residual mass convergences are set to 5.0×10^{-5} for gas and particle phases. The in-house source codes are written in Fortran 90 language, with the amount of statement being approximately 9600, in which the debug platform is the Compaq Visual Fortran. Experimental validations for the proposed model, algorithm, and code are carried out using a spherical glass bead with a diameter of $d_p = 56$ μm and a density of $\rho_p = 1545$ kg/m^3 in Sommerfeld's experiment.[6] The ultralight graphite particles with a density of $\rho_{gp} = 21.8$ kg/m^3 and five shapes of sphere, ideal, elongated cylinders, cubic, and elongated cuboid plates are numerically simulated. The equivalent diameters of $d_{ep} = 56$ μm with different sphericities ψ of 1.0, 0.94, 0.87, 0.72, and 0.63 are employed, and the schematic diagram of the coaxial combustor is shown in Figure 1. In this figure, the contour of the subfigure is the vortice distributions of spherical glass particles ($\psi = 1.0$), and those of nonspherical particles are being investigated.[47]

RESULTS AND DISCUSSION

The experimental validations are shown in Figure 2. We can see that the predicted particle axial and tangential fluctuation velocity are in good line with the measurement. Moreover, the annular-reversed flow region along with the axial direction and the Rankine-vortex structure along with the tangential

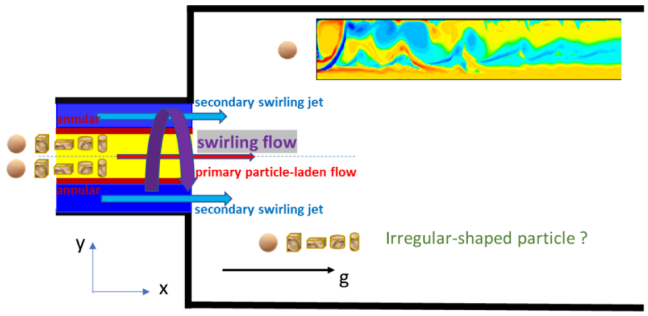

Figure 1. Schematic diagram of the coaxial combustor with irregular-shaped particles.

direction are captured, which are in good agreement with experiments. The deviations and errors are mainly caused by the limitation of the RANS algorithm due to the failure of obtaining the instantaneous flow information and coherent flow structure, as well as short of the advanced closure transport equations and the better understanding mechanism for multiphase turbulent flow.

Figure 3 shows the distributions of normalized number density of ultralight density particles. As seen from this figure, bimodal peaks at central axis regions along with the streamwise direction can be observed, and they are different with particle sphericities. At the near inlet region of $x = 52$ mm, the maximum values are the larger irregular-shaped particle with $\psi = 0.63$ and are decreased with particle sphericity with $\psi = 1.0$ toward the development flow direction. Furthermore, at the beginning section of $x = 112$ mm, the particles begin to move and accumulate at near wall regions as a result of the effects of tangential velocity, turbulent diffusion, and centrifugal force actions. Concentrations increased with the particle sphericity reaching up to the maximum values at the cross section of $x = 315$ mm for $\psi = 1.0$, especially larger than those of central regions. The reason is that ultralight density particles are easier to be thrown out of the central region and move to wall regions because of their smaller inertia compared with the heavy glass particles, which easily penetrate the primary central region because of their larger inertia. Furthermore, those particles with the higher irregular-shaped degrees are contributed to the acceleration accumulations near wall regions dined by interactions between gas and particle phases.

Figure 4 shows the distributions of axial and tangential particle velocities under different particle sphericities. It is noted that the negative velocities at the near centerline and wall recirculation regions and the tangential swirling velocity are generated. The bimodal peaks with W-shaped profiles are found at the inlet region, and they gradually evolved into a flat profile along with the streamwise direction thereafter. As a matter of fact, the lower density of the graphite particle is readily carried by gas turbulence, indicating that it has excellent followability with the gas phase, and the effects of gravity are relatively slight or negligible. In the meantime, these are always larger than those of glass beads in the experiment.[6] Lower sphericities of particles have larger peak values and exhibit the strongly anisotropic dispersions than those of higher sphericities; it can be explained that the drag force between the gas and irregular shape particle is dominant, and inlet effects are neglected because of their smaller inertia. The most important phenomenon observed is that the peak values of $\psi = 0.63$ and 0.72 are approximately 3.0 times larger than those sphericities located at near central regions (see Figure 4a). It is

https://doi.org/10.1021/acsomega.1c02053
ACS Omega 2021, 6, 16631−16640

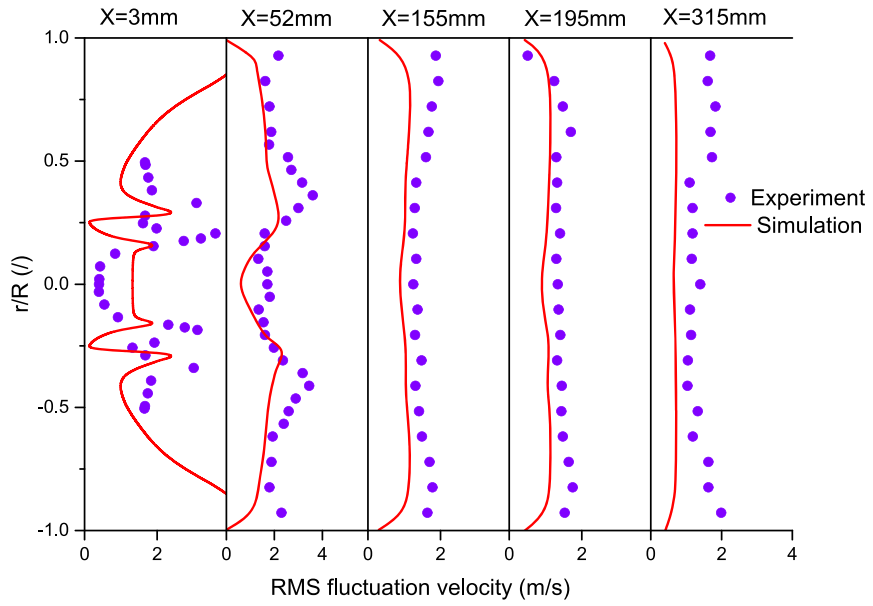

(a) axial direction

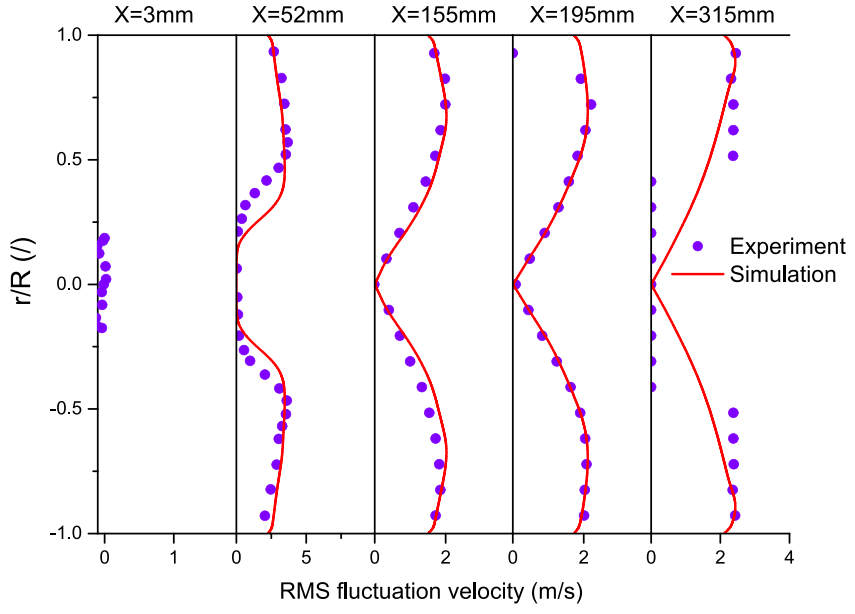

(b) tangential direction

Figure 2. Experimental validations for the axial and tangential RMS fluctuation velocity of the particle: (a) axial direction and (b) tangential direction.

demonstrated that the drag force for the higher irregular-shaped degree is far greater than the interlock force between particles and their own centrifugal force.[37−39]

Figure 5 shows the distributions of the root-mean-square axial and tangential particle fluctuation velocity at different particle sphericities. The fluctuation velocities of ψ = 0.63 and 0.72 are intensified along with streamwise flow because of a larger drag force. Compared to the inlet effects, the interactions between the gas and nonspherical particle and interlock forces are primary. Thus, the effects of sphericity play important roles in particle dispersions. We can see that the profiles of higher sphericity particle exhibit flat and uniform since their interlock forces are less than those of lower sphericity particles.[38,39] Lower sphericity ultralight particles are sensitive to followability by the gas phase rather than controlled by their own inertia leading to the complex transport characteristics.

Figure 6 reveals the distributions of the Reynolds stresses of particles along axial−axial and axial−tangential directions. They present the distinctively anisotropic characteristics resulting in the redistribution of the Reynolds stresses. As for spherical particles, large values are found at inlet shear regions induced by higher velocity gradients, and they are about 4.5 times larger than those of the fully development flows because of higher interlock force among nonspherical particles. Additionally, axial−axial values are larger than those of the axial−tangential direction. Compared to those of lower sphericities ψ = 0.63 and 0.72, these spherical particles are

https://doi.org/10.1021/acsomega.1c02053
ACS Omega 2021, 6, 16631−16640

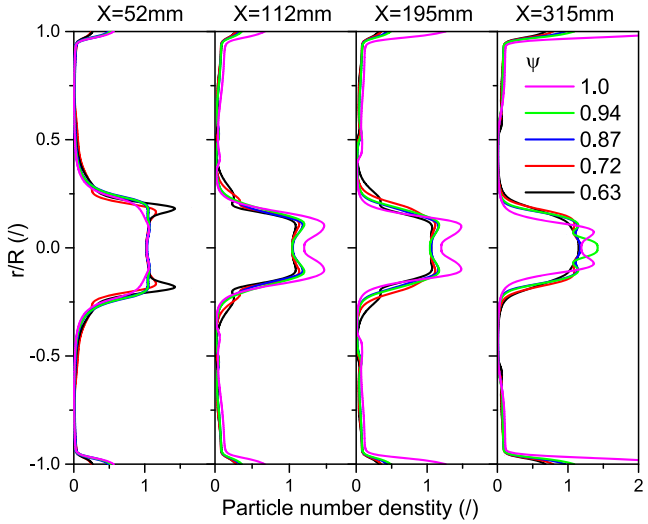

Figure 3. Distributions of normalized number density of ultralight density particles.

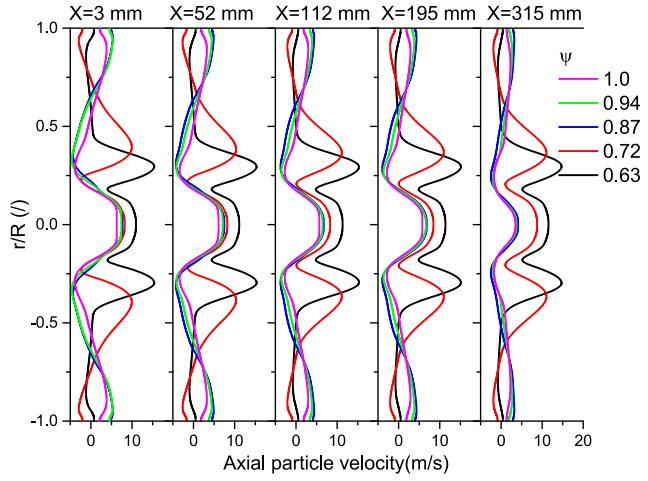

(a) axial direction

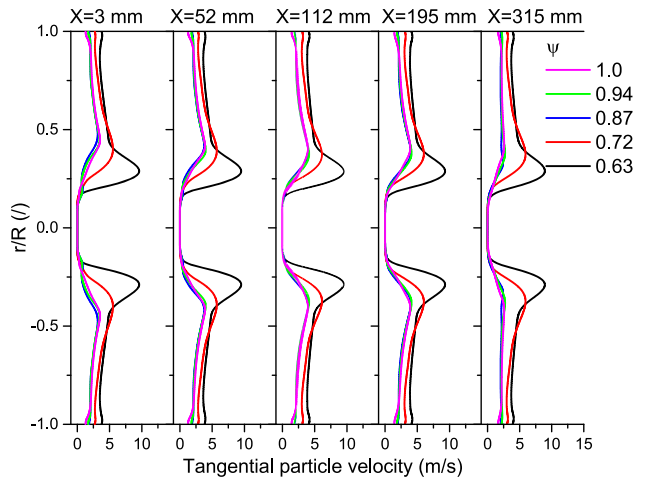

(b) tangential direction

Figure 4. Profiles of axial and tangential particle velocity: (a) axial direction and (b) tangential direction.

significantly higher because they are easier to penetrate the reversed-flow region and majority of particles preferentially

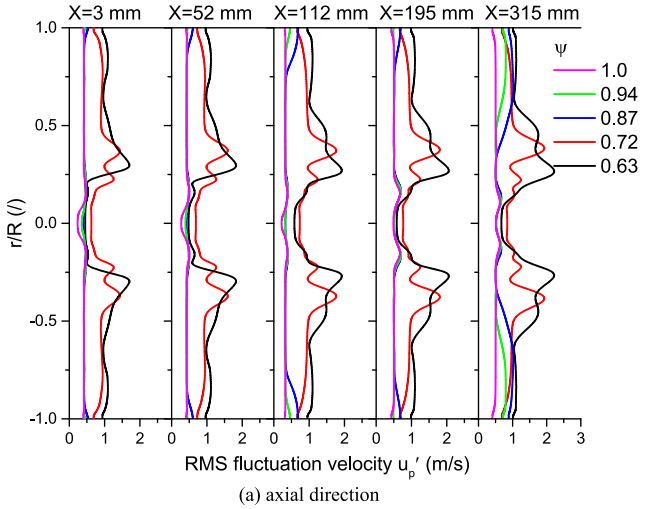

(a) axial direction

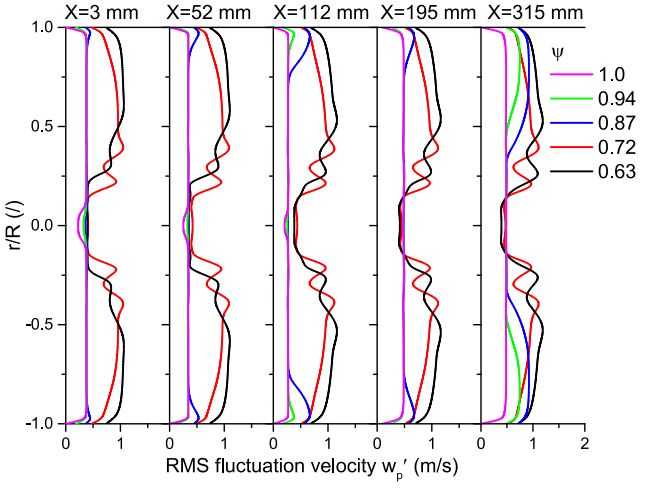

(b) tangential direction

Figure 5. Profiles of root-mean-square axial and tangential particle fluctuation velocity: (a) axial direction and (b) tangential direction.

accumulated along the shear layer. In other words, spherical particles are primarily affected by the inlet effects because of a relatively smaller drag force in comparison with an irregular-shaped degree.

Figure 7 shows the profiles of the Reynolds normal and shear stresses between the gas and particle along the axial−axial and tangential−axial directions, respectively. The distributions of axial−axial and axial−tangential with ψ = 0.63 and 0.72 have strong anisotropic characteristics, and their normal stress are approximately 3.4 times larger than those of the shear stress of the spherical particle. The reasons are that the irregular shape particle has larger drag forces between the gas and particle, resulting in poor followability behaviors, and the higher degree in nonsphericity enhances the anisotropic behaviors. The normal and shear stresses have different appearances under the complex effects of centrifugal forces, turbulent diffusions, and nonspherical degrees. The overlap sections in Figure 7b imply that the tangential−axial shear stress almost disappeared for high-sphericity particles away from central regions.

The profiles of the turbulent kinetic energy of particle are given in Figure 8. The nonspherical particles have the larger turbulent kinetic energy at far stream flow because of the

https://doi.org/10.1021/acsomega.1c02053
ACS Omega 2021, 6, 16631−16640

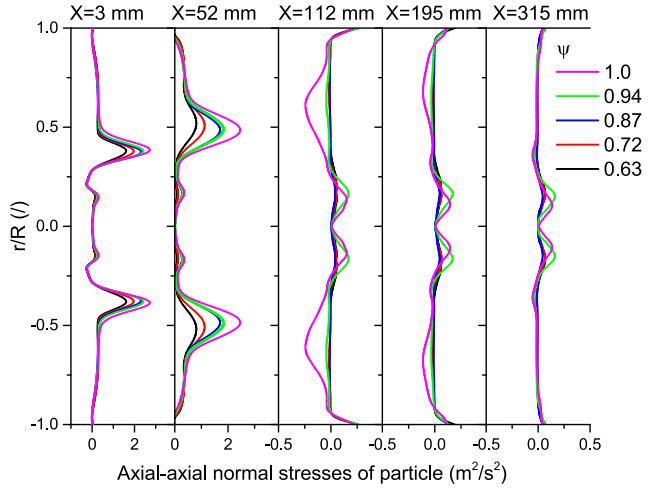

(a) axial-axial direction

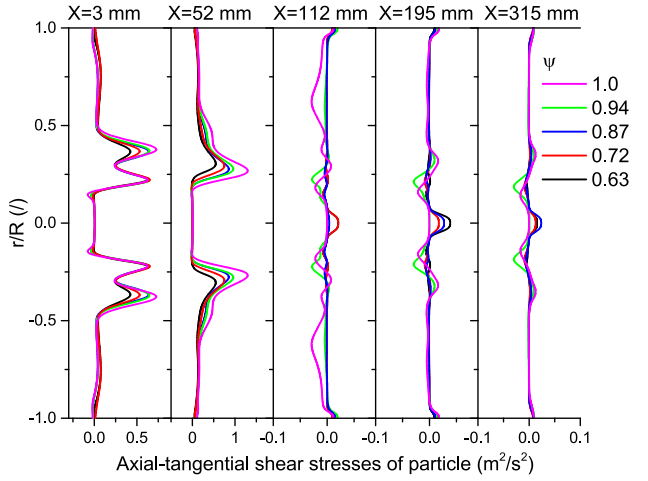

(b) axial-tangential direction

Figure 6. Profiles of Reynolds stresses of particles: (a) axial−axial direction and (b) axial−tangential direction.

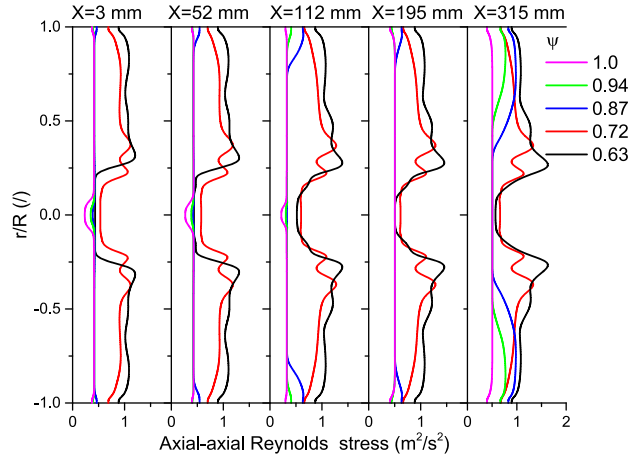

(a) axial-axial direction

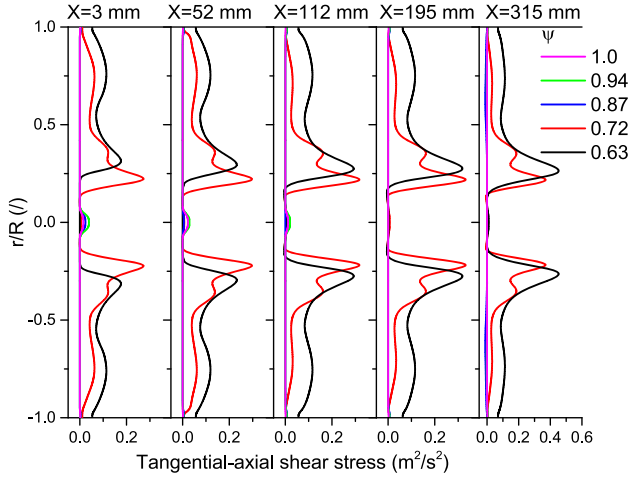

(b) tangential-axial direction

Figure 7. Profiles of root-mean-square Reynolds stresses between the gas and particle: (a) axial−axial direction and (b) tangential−axial direction.

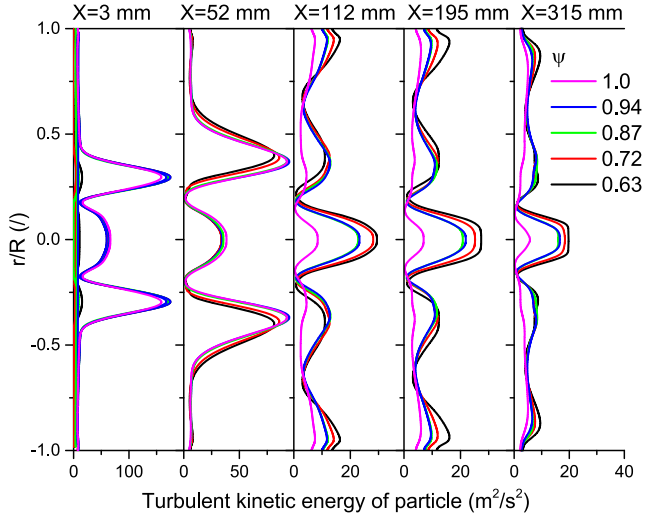

Figure 8. Profiles of the turbulent kinetic energy of particle.

higher interaction activities and fluctuation velocities between gas and particle phases. Under the conditions that the inlet effects on the sections of x = 3 and 52 mm are considered, their peak values are larger than those of fully development flow regions. Lower sphericities make more contributions to the enhancement when inlet effects are vanishing.

Figure 9 shows the vorticity maps of particle swirling flows under different sphericities. The evolution of the vortex shows that the shedding vortices from the inlet region were rolled up by the boundary layer with the vortices from the shear layer and then underwent a process of pairing, merging, and breakup. No distinct vortex can be observed because the axial particle flow is more rigid than the gas phase. The maximum values are generated at the location of central-reversed flow borders and shear layer zones. For the lower sphericity particles, the lengths of central and recirculation flow regions are elongated because of a larger drag force (see Figure 9e). The swirling flow structures of nonspherical particles are considerably complicated as a result of complex multiphase turbulent diffusions and momentum transfer interactions between the gas and particle and particle and particle. Anisotropic dispersions gradually evolved into the flat performances with the increasing sphericity.

CONCLUSIONS

In this work, the hydrodynamics of EGP two-phase swirling turbulent flow in the coaxial chamber was investigated using an

https://doi.org/10.1021/acsomega.1c02053
ACS Omega 2021, 6, 16631−16640

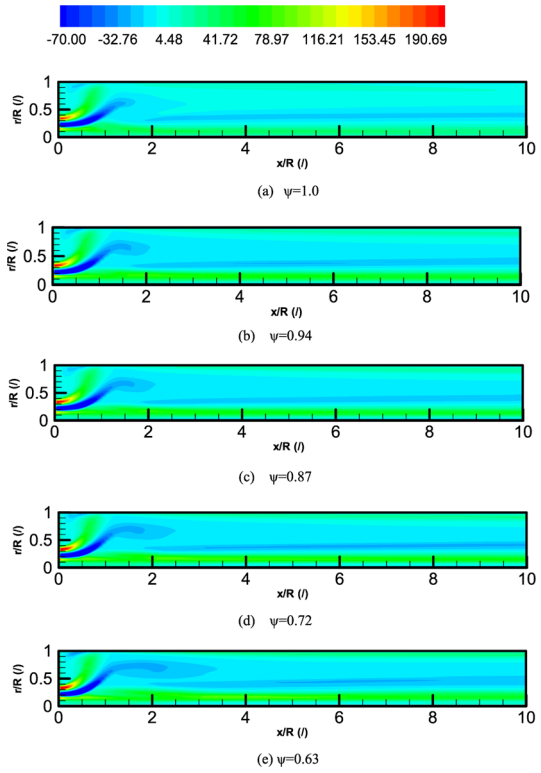

Figure 9. Distributions of the vorticities of particles at different sphericities (1/s): (a) ψ = 1.0, (b) ψ = 0.94, (c) ψ = 0.87, (d) ψ = 0.72, and (e) ψ = 0.63.

improved kinetic frictional stress model and an adopted drag coefficient to describe the momentum transfer between gas and nonspherical particle phases. The effects of particle sphericity on the ultralight particle dispersions were analyzed in detail. The proposed mathematical model, scientific codes, can predict accurately the graphite particle dispersions of the nonspherical particle−gas system in the chamber, and the influence of sphericity on the drag coefficient is very important. Particles with a lower sphericity show the stronger anisotropic characteristics of the particle velocities, the fluctuation velocities, and the Reynolds stresses. The interlock force between the nonspherical particle takes impediment for particle flows, which is greater than that of the spherical particle. The swirling flow structure of the nonspherical gas−particle system is affected by the complicated turbulent diffusion, momentum transfer, and interactions between the gas and particle phase. Further experimental validations for the different ranges of the Reynolds number and the comprehensive effects of the particle shape and size will be studied in future.

AUTHOR INFORMATION

Corresponding Authors

Yang Liu − *School of Aerospace Engineering, Taizhou University, Zhejiang 318000, China; Department of Engineering Mechanics, Tsinghua University, Beijing 10084, China;* orcid.org/0000-0003-3377-2130; Email: liuya@mail.tsinghua.edu.cn

Guohui Li − *School of Electronic and Information Engineering, Dalian Jiaotong University, Dalian 116028, China;* Phone: +1-984-269-9946; Email: maillgh@djtu.edu.cn

Authors

Yongju Zhang − *School of Aerospace Engineering, Taizhou University, Zhejiang 318000, China*

Li Zhang − *School of Aerospace Engineering, Taizhou University, Zhejiang 318000, China*

Complete contact information is available at: https://pubs.acs.org/10.1021/acsomega.1c02053

Author Contributions

The manuscript was written through the contributions of all authors. All authors have approved the revised version of manuscript.

Notes

The authors declare no competing financial interest.

ACKNOWLEDGMENTS

The authors would like to acknowledge the financial support from the National Key Research and Development Program of China (no. 2017YFC0702600).

NOMENCLATURE

C_D	drag coefficient (dimensionless)
d_p	diameter of particle (m)
D	diffusion term (kg/ms^3)
e_p	restitution coefficient of particle (dimensionless)
e_w	restitution coefficient of wall (dimensionless)
e_{eff}	effective particle coefficient (dimensionless)
f	friction (dimensionless)
g	gravitational acceleration (m/s^2)
g_0	radial distribution function (dimensionless)
$\mathbf{I}$	unit tensor (dimensionless)
k_g	turbulent kinetic energy of gas (m^2/s^2)
k_p	turbulent kinetic energy of particle (m^2/s^2)
m	mass flow rate (g/s)
p	thermodynamic pressure (Pa)
p_{p_f}	particle phase pressure (Pa)
p_p	particle frictional pressure (Pa)
P	production term (kg/ms^3)
Re_p	particle Reynolds number (dimensionless)
u_g	gas velocity (m/s)
u_p	particle velocity (m/s)
s	swirling number, (dimensionless)
t	time (s)
T	interaction term (dimensionless)

GREEK ALPHABETS

α_g	gas volume fraction (dimensionless)
α_p	particle concentration (dimensionless)
β_{pg}	interphase drag coefficient (dimensionless)
δ	Kronecker delta unit tensor (dimensionless)
ρ_g	gas density (kg/m^3)
ρ_p	particle density (kg/m^3)
ε_g	turbulent energy dissipation rate of gas (m^2/s^3)
ε_p	turbulent energy dissipation rate of particle (m^2/s^3)
μ_g	gas dynamic viscosity (Pa s)
μ_p	particle shear viscosity (Pa s)
τ_g	stress tensor of gas phase (Pa)
τ_p	stress tensor of particle phase (Pa)
τ_{rp}	particle relaxation time (s)
φ	sphericity, blending function (dimensionless)
ω_f	angle of internal friction (degree)
ψ	particle shape descriptor (dimensionless)

https://doi.org/10.1021/acsomega.1c02053
ACS Omega 2021, 6, 16631−16640

χ particle circularity (dimensionless)
θ granular temperature (m^2/s^2)
Π pressure−strain term (dimensionless)
Γ conductivity coefficient (kg/ms^3)
γ collisional dissipation rate, (kg/ms^3)
ξ_p particle bulk viscosity (Pa s)

SUPERSCRIPTS

′ fluctuation
− averaged

SUBSCRIPTS

i,j,k coordinate directions
g,p gas and particle
l laminar
m max

REFERENCES

(1) Crowe, C.; Sommerfeld, M. S.; Tsuji, Y. *Multiphase Flows with Droplets and Particles*; CRC Press: Boca Raton, 1998.
(2) Margadonna, S.; Prassides, K. *Encyclopedia of Materials: Science and Technology*; Pergamon Press: Oxford, U.K., 2001.
(3) Liu, Y.; Zhang, L.; Chen, Z. Y.; Zhou, L. X. Numerical investigation on mixture particle dispersion characteristics in swirling particle-laden combustion chamber. *Int. Commun. Heat Mass Transfer* **2020**, *117*, No. 104720.
(4) Liu, Y.; Chen, Z. Y.; Zhang, Y. J.; Zhou, L. X. Hydrodynamic modeling of swirling binary mixture gasp-article flows using a second order moment turbulence model. *ACS Omega* **2020**, *5*, 31490−31501.
(5) Liu, Y.; Jiang, L. X.; Zhang, Y. J. Hydrodynamic modeling of turbulence modulation by particles in a swirling gas-particle two-phase flow. *ACS Omega* **2021**, *6*, 10106−10118.
(6) Sommerfeld, M.; Qiu, H. H. Detailed measurements in a swirling particulate two-phase flow by a phase Doppler anemometer. *Int. J. Heat Fluid Flow* **1991**, *12*, 20−28.
(7) Sommerfeld, M.; Qiu, H. H. Characterization of particle-laden, confined swirling flows by a phase-doppler anemometer. *Int. J. Heat Fluid Flow* **1993**, *19*, 1093−1127.
(8) Sommerfeld, M.; Ando, A.; Wennerberg, D. Swirling, particle-laden flows through a pipe expansion. *J. Fluids Eng.* **1992**, *114*, 648−656.
(9) Kosiwczuk, W.; Cessou, A.; Trinite, M.; Lecordier, B. Simultaneous velocity field measurements in two-phase flows for turbulent mixing of sprays by means of two-phase PIV. *Exp. Fluids* **2005**, *39*, 895−908.
(10) Sciacchitano, A.; Wieneke, B.; Scarano, F. PIV uncertainty quantification by image matching. *Meas. Sci. Technol.* **2013**, *24*, No. 045302.
(11) Naz, M. Y.; Sulaiman, S. A.; Shukrullah, S.; Ghaffar, A. PIV investigations on particle velocity distribution in uniform swirling regime of fluidization. *Granular Matter* **2017**, *19*, No. 40.
(12) Liu, Y.; Li, G. H.; Jiang, L. X. Numerical simulation on antenna temperature field of complex structure satellite in solar simulator. *Acta Astronaut.* **2009**, *65*, 1098−1106.
(13) Gillandt, I.; Fritsching, U.; Bauckhage, K. Measurement of phase interaction in dispersed gas/particle two-phase flow. *Int. J. Multiphase Flow* **2001**, *27*, 1313−1332.
(14) Fessler, J. R.; Eaton, J. K. Turbulence modification by particles in a backward-facing step flow. *J. Fluid Mech.* **1999**, *394*, 97−117.
(15) Lu, H. L.; He, Y. R.; Liu, Y.; Bir, R. S.; Liu, W. T. Numerical simulation of multi-component dense gas-solid flow. *J. Eng. Thermophys.* **2002**, *23*, 369−371.
(16) Liu, Y.; Lu, H. L.; Liu, W. T. Model and simulation of gas-solid flow with wide size distributions in circulating fluidized bed. *J. Chem. Ind. Eng.* **2003**, *54*, 1065−1071.
(17) Li, X. L.; Lv, S. H.; Liu, Y. Effects of particle-particle collisions on sudden expansion gas-particle flows via a two-phase kinetic energy-particle temperature model. *Adv. Powder Technol.* **2013**, *24*, 98−105.
(18) Liu, Y.; Li, G. H. Investigations of gas-particle two-phase flow in swirling combustor by the particle Stokes numbers. *Processes* **2021**, *9*, No. 951.
(19) Liu, Y.; Li, G. H.; Li, X. L.; Zhou, L. X. Investigation on ultralight particle dispersions in dense two-phase flow using a kinetic friction stress model. *Case Studies Thermal Eng.* **2021**, *26*, No. 101096.
(20) Hoomansm, B. P. B.; Kuipers, J. A. M.; Briels, W. J.; Van Swaaij, W. P. M. Discrete particle simulation of bubble and slug formation in a two-dimensional gas-fluidised bed: A hard-sphere approach. *Chem. Eng. Sci.* **1996**, *51*, 99−108.
(21) Xu, B. H.; Yu, A. B. Numerical simulation of the gas-solid flow in a fluidized bed by combining discrete particle method with computational fluid dynamics. *Chem. Eng. Sci.* **1997**, *52*, 2785−2809.
(22) Yuu, S.; Nishikawa, H.; Umekage, T. Numerical simulation of air and particle motion in group-B particle turbulent fluidized bed. *Powder Technol.* **2001**, *118*, 32−44.
(23) Zhou, H. S.; Flamant, G. D.; Gauthier, J. D.; Lu, J. Lagrangian approach for simulating the gas-particle flow structure in a circulating fluidized bed riser. *Int. J. Multiphase Flow* **2002**, *28*, 1801−1821.
(24) Helland, E.; Occeli, R.; Tadrist, L. Computational study of fluctuating motions and cluster structures in gas-particle flows. *Int. J. Multiphase Flow* **2002**, *28*, 199−223.
(25) Pakhomov, M. A.; Terekhov, V. I. Structure of the nonisothermal swirling gas-droplet flow behind an abrupt tube expansion. *Fluid Dyn.* **2016**, *51*, 70−80.
(26) Liu, Y.; Zhang, L.; Zhou, L. X. Effects of swirling flow on ultralight particle dispersion characteristics in coaxial jet combustor. *Energy Sci. Eng.* **2019**, *7*, 3220−3233.
(27) Apte, S. V.; Mahesh, K.; Moin, P.; Oefelein, J. C. Large-eddy simulation of swirling particle-laden flows in a coaxial-jet combustor. *Int. J. Multiphase Flow* **2003**, *29*, 1311−1133.
(28) Oefelein, J. C.; Sankaran, V.; Drozda, T. G. Large eddy simulation of swirling particle laden flow in model axisymmetric combustor. *Proc. Combust. Inst.* **2007**, *31*, 2291−2299.
(29) Yan, J.; Gui, N.; Xie, G. N.; Gao, J. S. Direct numerical simulation of particle-laden swirling flows on turbulence modulation. *Math. Probl. Eng.* **2014**, *3*, 1−12.
(30) Zastawny, M.; Mallouppas, G.; Zhao, F.; Van Wachem, B. Derivation of drag and lift force and torque coefficients for non-spherical particles in flows. *Int. J. Multiphase Flow* **2012**, *39*, 227−239.
(31) Ouchene, R.; Khalij, M.; Arcen, B.; Tanière, A. A new set of correlations of drag, lift and torque coefficients for non-spherical particles and large Reynolds numbers. *Powder Technol.* **2016**, *303*, 33−43.
(32) Sanjeevi, K. P.; Kuipers, J. A. M.; Padding, J. T. Drag, lift and torque correlations for non-spherical particles from Stokes limit to high Reynolds numbers. *Int. J. Multiphase Flow* **2018**, *106*, 325−337.
(33) Ilie, M. Numerical studies of turbulent swirling reacting flows using LES and URANS. *Int. J. Therm. Sci.* **2018**, *134*, 89−100.
(34) Li, J. P.; Zhou, F.; Yang, D. L.; Yu, B.; Li, Y. Effect of swirling flow on large coal particle pneumatic conveying. *Powder Technol.* **2020**, *362*, 745−758.
(35) Knoll, M.; Gerhardter, H.; Tomazic, P.; Hochenauer, C. Investigations of lateral particle distribution for spherical and highly non-spherical particles by means of steady-state/transient RANS and LES simulations. *Powder Technol.* **2021**, *378*, 618−638.
(36) Gao, X.; Li, T.; Sarkar, A.; Lu, L.; Rogers, W. Development and validation of an enhanced filtered drag model for simulating gas-solid fluidization of Geldart a particle in all flow regimes. *Chem. Eng. Sci.* **2018**, *184*, 33−51.
(37) Yan, S. N.; He, Y. R.; Tang, T.; Wang, T. Drag coefficient prediction for nonspherical particles in dense gas-solid two-phase flow using artificial neural network. *Powder Technol.* **2019**, *354*, 115−124.
(38) Yan, S. N.; Wang, T. Y.; Tang, T. Q.; Ren, A. X.; He, Y. R. Simulation on hydrodynamics of non-spherical particulate system

https://doi.org/10.1021/acsomega.1c02053
ACS Omega 2021, 6, 16631−16640

using a drag coefficient correlation based on artificial neural network. *Pet. Sci.* **2020**, *17*, 537−555.
(39) Vollmari, K.; Jasevicius, R.; Emden, H. Experimental and numerical study of fluidization and pressure drop of spherical and non-spherical particles in a model scale fluidized bed. *Powder Technol.* **2016**, *291*, 506−521.
(40) Kruggel, H. E.; Vollmari, K. Flow-regime transitions in fluidized beds of nonspherical particles. *Particuology* **2016**, *29*, 1−15.
(41) Mahajan, V. V.; Padding, J. T.; Nijssen, T. M. J.; Buist, K. A.; Kuipers, J. A. M. Nonspherical particles in a pseudo-2D fluidized bed: Experimental study. *AIChE J.* **2018**, *64*, 1573−1590.
(42) Zhou, L. X. Two-fluid turbulence modeling of swirling gas-particle flows-A review. *Powder Technol.* **2017**, *314*, 253−263.
(43) Liu, Y.; Zhang, Y. J.; Zhou, L. X. Numerical study on bubble-liquid two-phase turbulent hydrodynamics in extremely narrow shape bioreactor. *Int. Commun. Heat Mass Transfer* **2019**, *108*, No. 104286.
(44) Liu, Y.; Zhou, L. X.; Zhang, Y. J. Numerical simulation of bubble-liquid two-phase turbulent flows in shallow bioreactor. *Energies* **2019**, *12*, 2269−2282.
(45) Liu, Y.; Zhang, L.; Zhou, L. X. Development of modeling and simulation of bubble liquid hydrodynamics in bubble column. *Energy Sci. Eng.* **2020**, *8*, 327−339.
(46) Liu, Y.; Zhang, L.; Zhang, Y. J.; Zhou, L. X. Effects of sparger holes on gas-liquid hydrodynamics in bubble column. *Chem. Eng. Technol.* **2020**, *43*, 307−316.
(47) Liu, Y.; Zhou, L. X.; Xu, C. X. Numerical simulation of instantaneous flow structure of swirling, and non-swirling coaxial jet particle laden turbulence flows. *Phys. A (Amsterdam, Neth.)* **2010**, *389*, 5380−5389.

https://doi.org/10.1021/acsomega.1c02053
ACS Omega 2021, 6, 16631−16640